Pergamon

PII: S0045-7930(96)00047-3

Computers & Fluids Vol. 26, No. 4, pp. 321–337, 1997

Printed in Great Britain
0045-7930/97 $17.00 + 0.00

TOPOLOGICAL FLOW STRUCTURES IN BACKWARD-FACING STEP CHANNELS

T. P. CHIANG, TONY W. H. SHEU* and S. F. TSAI

Department of Naval Architecture and Ocean Engineering, National Taiwan University, 73 Chou San Road, Taipei, Taiwan, R.O.C.

(Received 21 May 1996; in revised form 5 September 1996)

Abstract—The present paper is intended to solve the steady-state Navier–Stokes equations for different Reynolds numbers. Through out this paper, the incompressible fluid will be considered in three-dimensional channels with different spans. The flow field under investigation was characterized as having a backward-facing step across which a fully-developed three-dimensional channel flow expanded into the channel with an expansion ratio of 1.9432. Numerical solutions for this backward-facing step problem were obtained on the basis of the step height, 0.9423, various spans, taking on values up to 10, and Reynolds numbers as high as 800. Of the different flow conditions that were considered, we elaborate on the flow topology under the conditions of an intermediate Reynolds number, $Re = 389$, and the largest width of the channel, 10. Following Lighthill [Lighthill, M., Attachment and separation in three-dimensional flow. In *Laminar Boundary Layers*, Vol. 2(6), ed. L. Rosenhead, II. Oxford University Press, 1963, pp. 72–82.] [1], we apply topology theory, which provides a rigorous mathematical foundation for studying kinematically possible flows. The present computational results, together with the inferred flow topology, reveal details of the flow structure which suggest a mechanism for the development of strongly three-dimensional flow with increasing Reynolds numbers. The computation of 'oil-flow' streamlines improves the visualization of the flow field and helps sketch the complicated flow patterns by clarifying the three-dimensional flow separation just behind the step. The scope of this enhancement to improved visualization of flow structure is also extended to the flow reattachment on the floor as well as the roof recirculatory flow pattern, manifested itself by the upstream separation and downstream reattachment surfaces. Notably addressed is the separation–reattachment phenomenon emanating only from the roof near the two side walls. © 1997 Elsevier Science Ltd.

1. INTRODUCTION

Flow reversals found in heat exchangers, ducts for industrial use, flows around buildings, and microelectronic circuit boards are considered among the most important factors in designing a fluid engineering device. Among this class of flows, the flow over a backward-facing step represents the problem which has the simplest geometry but, nonetheless, can provide separation and reattachment of the flow. This flow can be regarded as an entry flow in a channel with two parallel walls, a roof and a floor, followed by a confined recirculating flow behind a rearward-facing step. This expansion flow has attracted a great deal of attention over the last few decades and has been the subject of an international workshop [2]. The reasons for this problem having received considerable attention are two-fold. Firstly, this problem is rich in flow physics and is, thus, physically as well as practically important. Within the physical domain, the flow is characterized as having a shear layer separated from the step edge, a region of recirculating flow just behind the step, followed by a region of recirculating separation–reattachment flow attached to the roof of the channel, and a gradual development of the channel flow further downstream. Gaining a knowledge of this expansion flow is, thus, of importance in understanding shear stresses and heat transfer rates in many industrial flows. Experimental evidence has revealed the formation of a series of trailing vortices for the flow into the expansion downstream of the step. Detecting these separation eddies presents a challenging task for numerical algorithms. In this regard, we also consider this problem computationally important since it serves as a prototype for assessment of numerical models of incompressible viscous flows.

Physical importance has stimulated a number of experimental calibrations [3–10], among which, the experimental data obtained by Armaly *et al.* [4] are most frequently referenced. The wealth of experimental data permitted a very detailed comparison to be performed, with an emphasis on the two-dimensional context [2, 11]. Comparatively few studies have focused on three-dimensional

*Corresponding author (Fax + 886 2 3929885).

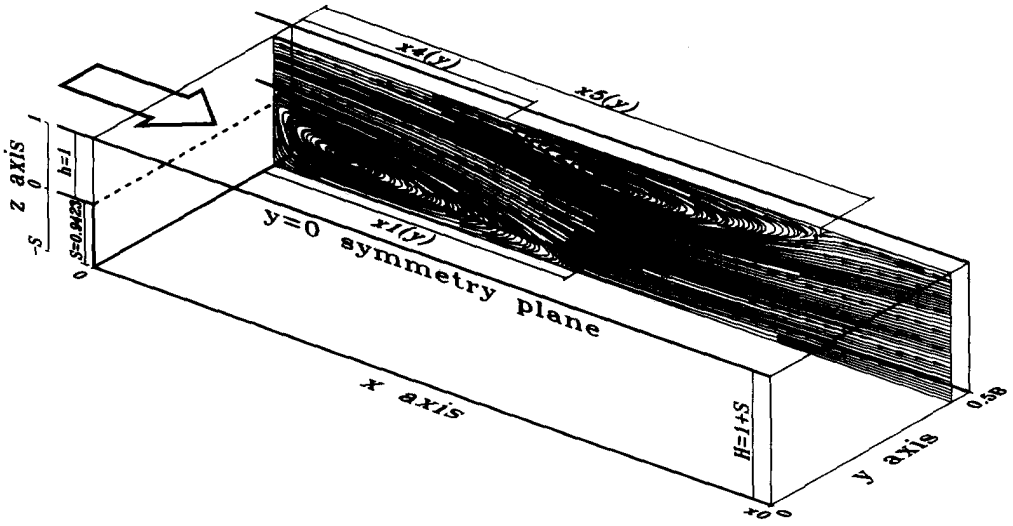

Fig. 1. Definition of the separation and reattachment lengths and the geometry of the investigated three-dimensional channel with a backward-facing step.

simulations [3, 12–16], and this fact motivated us to conduct this study. While previous efforts have shed light on some fundamental features of the backward-facing step flow, questions still remain unanswered, such as the broad pattern of the recirculating flow structure behind the step. The present work is directed towards exploring the three-dimensional expansion flow structure. Also, we address the flow physics behind the expansion step in great detail by adopting a topological theory on studying the computed three-dimensional vector field.

The remaining sections of this paper are organized as follows: working equations and the problem specifications are given in Section 2. This is followed by a brief outline of the segregated type algorithm, which is devised to compute the finite volume discretization equations iteratively. To present a clear picture of the vortical flow structure, we shall address the limiting streamlines or skin-friction lines as the target vector field by appealing to the theory of topology. The numerical results, together with the validation study, and conclusions are presented in the remaining sections. With the finite volume solutions thus obtained, a topological study on these detailed computed velocity vectors provides insight into the evolution of vortical flows as Reynolds numbers and width of the channel vary.

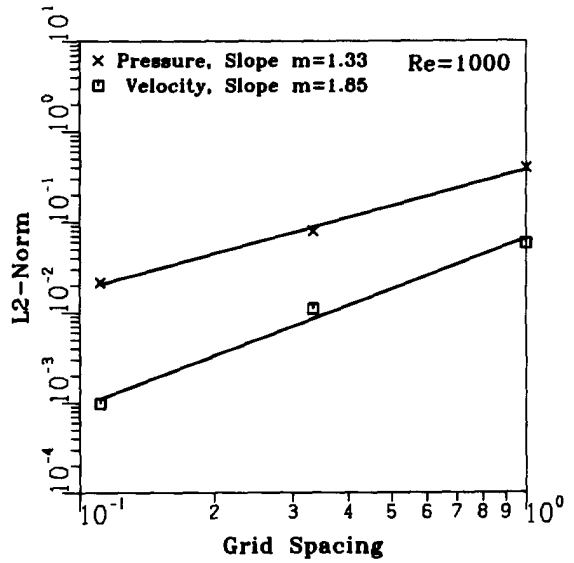

Fig. 2. Grid convergence test for the steady-state Navier–Stokes equations. The rate of convergence test is computed on the basis of grid sizes $2/n$, where $n = 2, 6, 18, 54$.

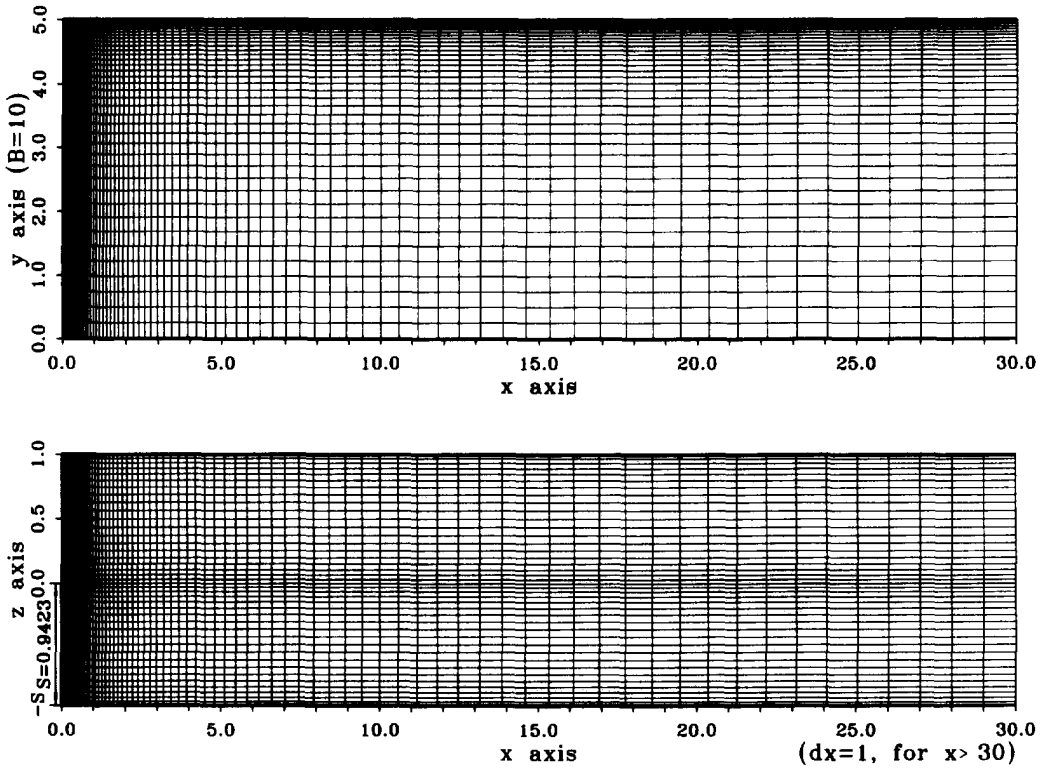

Fig. 3. An illustration of stretched grids.

2. WORKING EQUATIONS AND PROBLEM SPECIFICATIONS

In the absence of body force, we consider here the Newtonian fluid of kinematic viscosity v. Working equations consist of the Navier–Stokes equations of motion, which are subjected to the incompressibility constraint condition. Numerical modeling was performed under conditions pertaining to the following assumptions: (1) steady; (2) laminar:

$$\frac{\partial}{\partial x_m}(u_m u_i) = \frac{\partial p}{\partial x_i} + \frac{1}{Re}\frac{\partial^2 u_i}{\partial x_m \partial x_m} \tag{1}$$

$$\frac{\partial u_i}{\partial x_i} = 0\,. \tag{2}$$

In the above dimensionless primitive-variable equations, we denote u_i as the velocity components ($i = 1 \sim 3$), and p as the isotropic pressure. According to Fig. 1, the Reynolds number, Re, is defined as $Re = u_{\text{mean}}(2h/v)$; here, all lengths are normalized by h, the height of the upstream channel while all the velocities are normalized by the inlet mean velocity, u_{mean}, which is the result of an entry flow in a rectangular straight channel with cross-sectional area $h \times B$.

The rationale behind adopting the velocity–pressure formulation is that this setting can offer well-posed closure boundary conditions. As stated earlier, a fully-developed three-dimensional velocity profile is prescribed at the step, behind which the flow experiences an abrupt change in cross-sectional area of the channel. According to the work of Kaiktsis *et al.* [3], the upstream location where the inlet velocity profile is applied has no appreciable influence on the developed expansion flow as long as the Reynolds number is larger than 200. For $Re \leq 200$, the reattachment length of the salient corner vortex behind the step is overpredicted by almost 10% if the inflow boundary is taken exactly at the step expansion. Referring to Fig. 1, no-slip boundary conditions for velocities u_i are specified everywhere except at the physical inlet and the synthetic outlet. No pressure boundary condition is permitted; otherwise, the problem under consideration will be overdetermined. The effect of the truncated length on the channel flow has been investigated by Kaiktsis *et al.* [3]. For Reynolds numbers much lower than 700, the flow varies very little, as compared with solutions computed in the case with the channel lengths of $x_0 = 34$ and 60.

As to the value of the reattachment length, a difference of approximately 2% was reported in cases when $Re \geq 700$. We consider here the floating outflow boundary condition at a synthetic plane. Depending on the Reynolds numbers investigated, synthetic planes are truncated at different lengths downstream of the step.

Further work is in progress in an effort to mimic the physical experiment of Armaly *et al.* [4], where the upstream step height is 0.9423, and the width of the channel is 36. Here, we consider only the flow in a channel with two parallel walls with a much smaller spanwise length between them. Four widths are considered with the maximum set to 10.

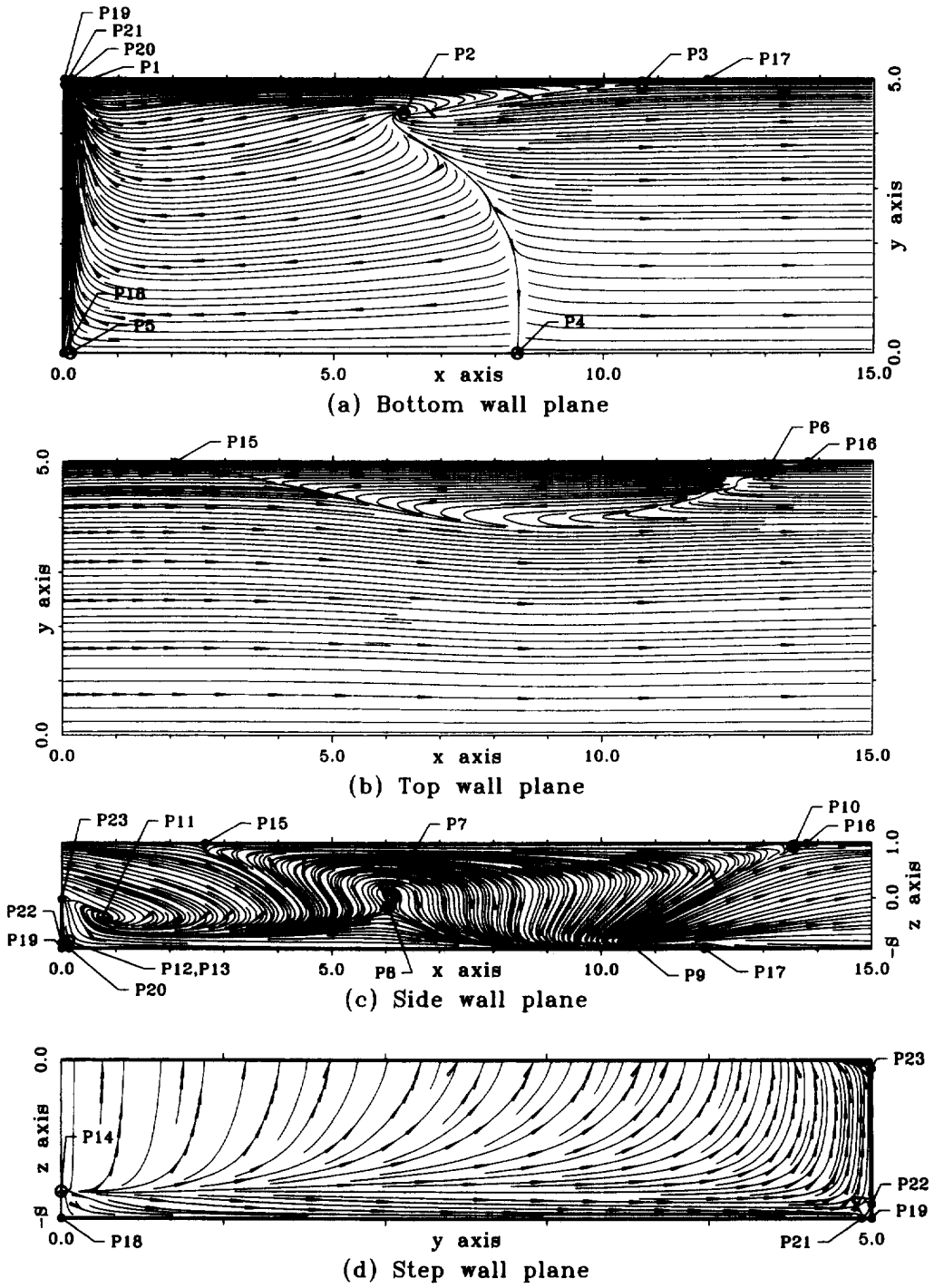

Fig. 4. The computed limiting streamlines on the floor, roof, end wall, and the step plane for the case of $Re = 389$, $B = 10$. Both locations and classification of symbols P1 ~ P23 are included in Table 1.

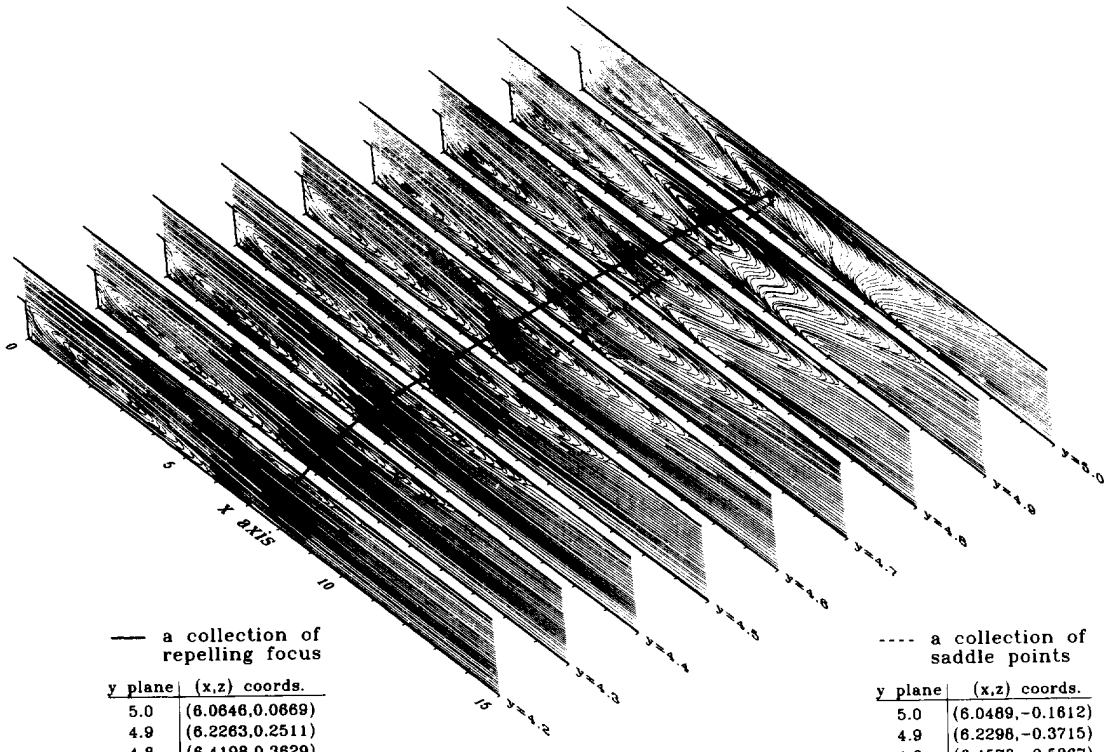

— a collection of repelling focus

y plane	(x,z) coords.
5.0	(6.0646,0.0669)
4.9	(6.2263,0.2511)
4.8	(6.4198,0.3629)
4.7	(6.6440,0.4565)
4.6	(6.9010,0.5360)
4.5	(7.2073,0.5936)
4.4	(7.5501,0.6619)
4.3	(8.0192,0.7170)
4.2	(8.7822,0.7769)

---- a collection of saddle points

y plane	(x,z) coords.
5.0	(6.0489,-0.1612)
4.9	(6.2298,-0.3715)
4.8	(6.4578,-0.5367)
4.7	(6.6779,-0.7173)
4.6	(6.8962,-0.8932)

Fig. 5. A three-dimensional plot of saddle points and repelling foci for the case of $Re = 389$ and $B = 10$.

3. FINITE VOLUME METHOD AND SOLUTION ALGORITHM

We now turn to transforming working equations into their algebraic counterparts which are amenable to computer simulation. To alleviate the well-known even–odd pressure oscillations for problems defined at the incompressible limit, we advocate the use of staggered grids following the findings of Harlow and Welch [17]. The grid used is one that offsets the velocities half a mesh size in their respective coordinate directions from the pressure. While a staggered mesh adds considerably to the programming, this grid setting is in widespread use for incompressible analyses because the enforcement of the compatibility condition, which is demanded to suppress pressure oscillations, is avoided.

Use of primitive variables to simulate incompressible Navier–Stokes equations may further complicate the analysis in the solution step. These complications are attributable to the absence of pressure unknowns in the continuity equation. Not only will this absence tend to increase the condition number for the discrete system, but it will also yield more zero diagonals, thus deteriorating the diagonal dominance. This presents a fundamental difficulty in solving algebraic equations using iterative solution solvers. A segregated solution algorithm comes naturally as a compensation to the mixed formulation. The algorithmic idea of the segregated approach is rooted in analyzing the working equations in a strongly decoupled fashion. Enforcement of the continuity equation is accomplished through the pressure, which is cast in a Poisson equation. This equation provides a mechanism for incorporating the incompressibility constraint into the formulation through multiply-staged equations. Such a pressure-correction algorithm can be regarded as a complement to the mixed formulation by considerably reducing the storage demand for matrix equations encountered. Without loss of stability, the semi-implicit scheme of SIMPLE [18], as applied to the present study, provided the same steady-state solution at less computational cost than did the equivalent explicit scheme.

False diffusion error is another class of numerical difficulty in predicting solutions for (1) and

(2). Under conditions where grid lines are increasingly skew to streamlines, the simulation quality deteriorates by the introduction of false diffusion errors, grossly polluting the flow physics over the entire domain. Deterioration of accuracy is particularly severe under high Reynolds number circumstances. To remedy this defect, nonlinear advective fluxes can be discretized by the use of an upwind-biased scheme. We apply here the QUICK scheme of Leonard [19] formulated in the nonuniformly discretized context. As was the case with the elliptic problem, both diffusive fluxes and pressure gradients are approximated by a second-order centered scheme. Also, discretization errors, as a result of invoking a curvilinear coordinate transformation, are generally considerable and hard to resolve for configurations involving an abrupt change or for curvilinear lines having appreciable curvature. As a consequence, we conduct the analysis here in a Cartesian coordinate system.

4. VALIDATION OF COMPUTER CODE

The first step in numerical exploration of flow physics is to validate the analysis code employed. Numerical verification of the computer code is indispensable. In this regard, we first consider here the validation problem defined in a cubic Ω ($-1 \leq ,x,y,z \leq 1$). Solutions to equations (1) and (2), subject to boundary conditions, are given as follows [20]:

$$\begin{aligned} u &= -a[e^{ax}\sin(ay \pm dz) + e^{az}\sin(ax \pm dy)] \\ v &= -a[e^{ay}\sin(az \pm dx) + e^{ax}\sin(ay \pm dz)] \\ w &= -a[e^{az}\sin(ax \pm dy) + e^{ay}\sin(az \pm dx)]. \end{aligned} \tag{3}$$

In this study we consider $a = d/2 = \pi/4$ and $Re = 1000$. The employed QUICK-type upwind

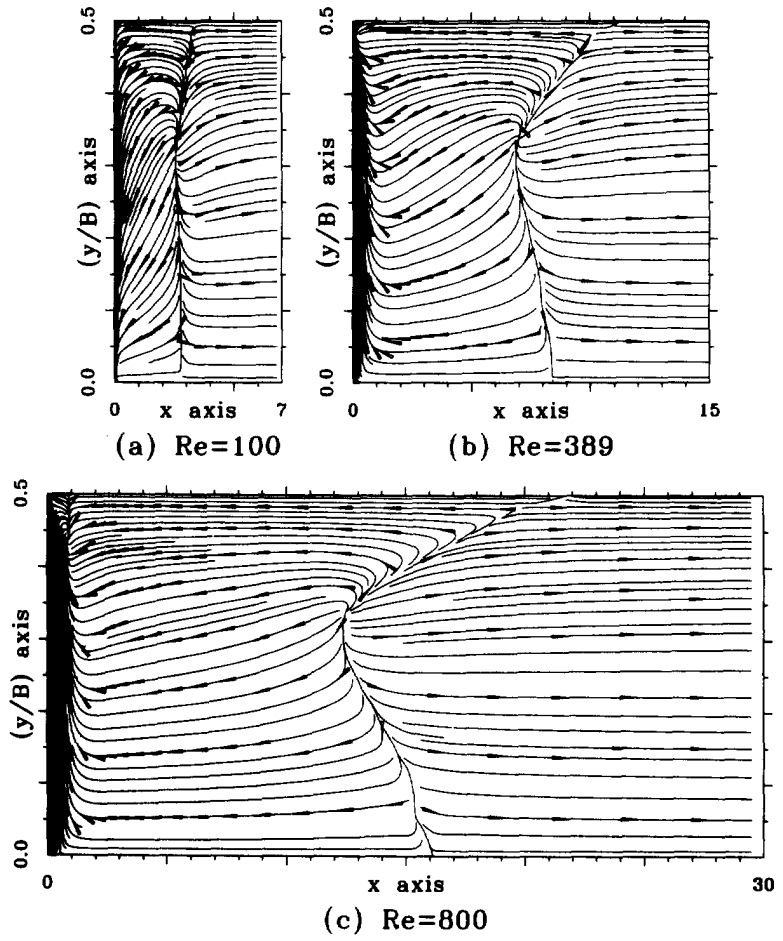

Fig. 6. The computed limiting streamlines on the floor of the channel for the case of $B = 4$. (a) $Re = 100$; (b) $Re = 389$; (c) $Re = 800$.

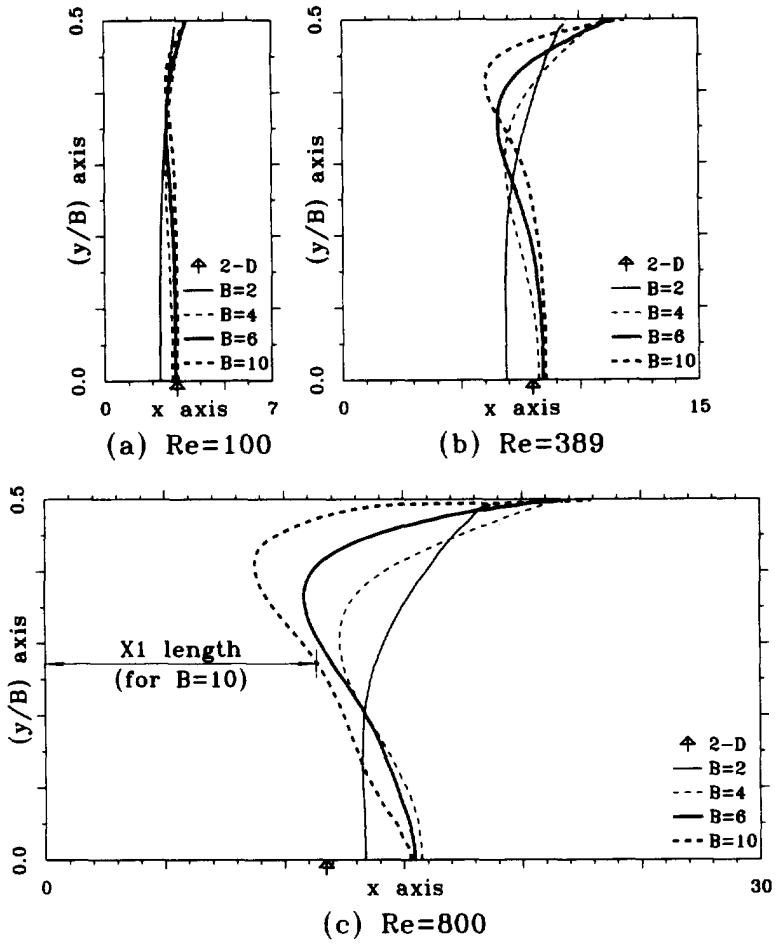

Fig. 7. The computed reattachment lengths x_1 against y for different spans and Reynolds numbers. (a) $Re = 100$; (b) $Re = 389$; (c) $Re = 800$.

discretization scheme and semi-implicit solution algorithm are assessed by measuring nodal errors cast in an L_2-norm form. With continuous refinement of grid spacings, we can compute the rate of convergence. According to the errors computed against the grid spacings, namely $h = 1,1/3,1/9,1/27$, the rates of convergence can be clearly seen in Fig. 2. This test, taking the solutions computed on the basis of $h = 1/27$ as exact, confirms the validity of the analysis code and provides us with sufficient confidence to proceed with analysis of three-dimensional expansion flow over a step.

5. TOPOLOGICAL STUDY ON THREE-DIMENSIONAL FLOW STRUCTURE

With the ever increasing speed of computers and the cost effectiveness of computational analyses, three-dimensional computations have become currently feasible. This has given rise to a renewed interest in visualizing much more complex three-dimensional vector fields. Three-dimensional vector fields are difficult to visualize using conventional methods. This difficulty has prompted researchers to develop new methodologies which provide a better description of the pertinent flow structure. There exist several methods to choose from. Notably use of graphical representations of the flow field, based on the helicity [21] and topology theory of continuous vector fields [1, 22], has been justified to achieve this goal and has gained wide acceptance. For a historical survey and the justification of their use, see Yates and Chapman [23] for additional details.

To explore the kinematics of a fluid flow, we have choices to adopt a qualitative theory of differential equations. This approach stems from the work of Poincare [24], who related the differential equations to the topology of vector fields. The idea behind the topological study of three-dimensional vector fields is to expand a given vector, $\mathbf{f}$, with respect to a specific point $\underline{\mathbf{x}}^0$,

known as the singular point. By definition, singular points are those points where $f_i|_{\underline{x}=\underline{x}_0=0}$. Given this fact, the Taylor series expansion of $\underline{\mathbf{f}}$ about $\underline{\mathbf{x}}^0$ is as follows:

$$f_i = (x_j - x_j^0)\frac{\partial f_i}{\partial x_j} + h.o.t.$$

Provided that the vector field $\underline{\mathbf{f}}$ is sufficiently smooth and differentiable, the eigenvalues and the associated eigenvectors of the matrix $\partial\underline{\mathbf{f}}/\partial\underline{\mathbf{x}}$ determine the behavior of $\underline{\mathbf{f}}$ around the singular point $\underline{\mathbf{X}}^0$. Depending on the sign of the eigenvalues, positive values indicate the repulsion of $\underline{\mathbf{f}}$ away from $\underline{\mathbf{x}}^0$ and negative values indicate the opposite [25]. The vector field spirals in or out of the singular point in cases where eigenvalues are classified as complex conjugate. The sign of the real part further classifies the portrait of the spirals.

Application of the qualitative theory of differential equations to fluid dynamics was done first by Lighthill [1], who chose skin-friction lines as the content of vector field. This work is an extension of the work of Legendre [22], who took, instead, streamlines into consideration for the topological study. Topological study on vector fields is featured by its mathematically rigorous foundation. The flow topology rendered from skin-friction lines corresponds to the experimental oil streak on the surface. Thanks to the theorem, which shows that limiting streamlines are equivalent to skin-friction lines, we can conduct topological studies on limiting streamlines. Besides visualizations conducted on the basis of the vector field, three-dimensional flows can also be sketched by means

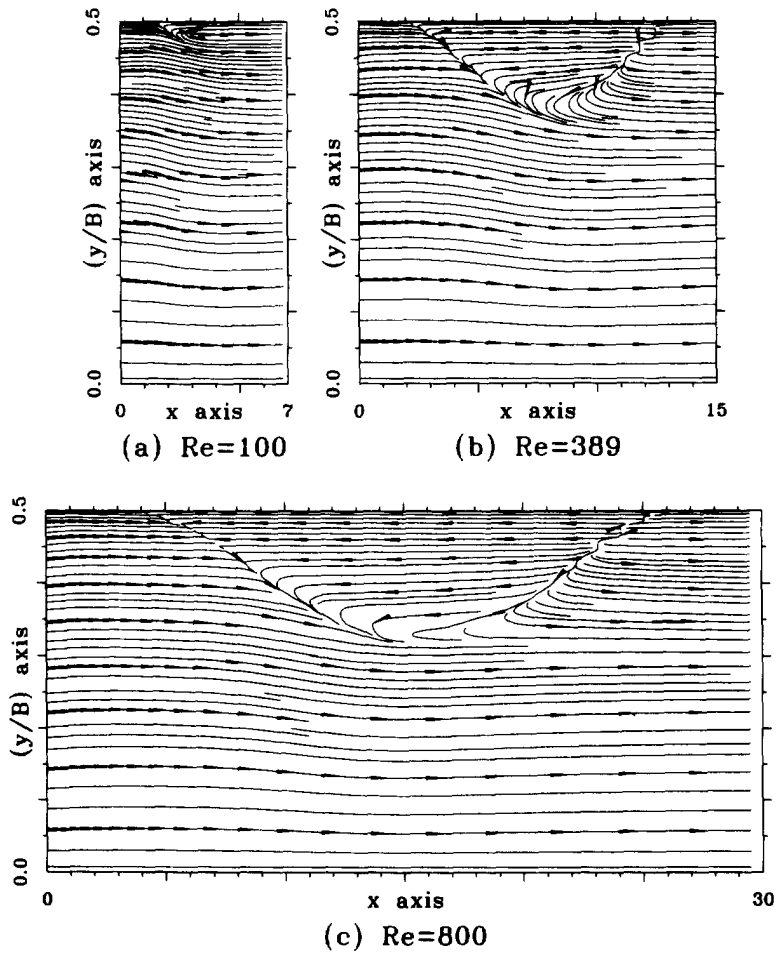

Fig. 8. The computed limiting streamlines on the roof of the channel for the case of $B = 6$. (a) $Re = 100$; (b) $Re = 389$; (c) $Re = 800$.

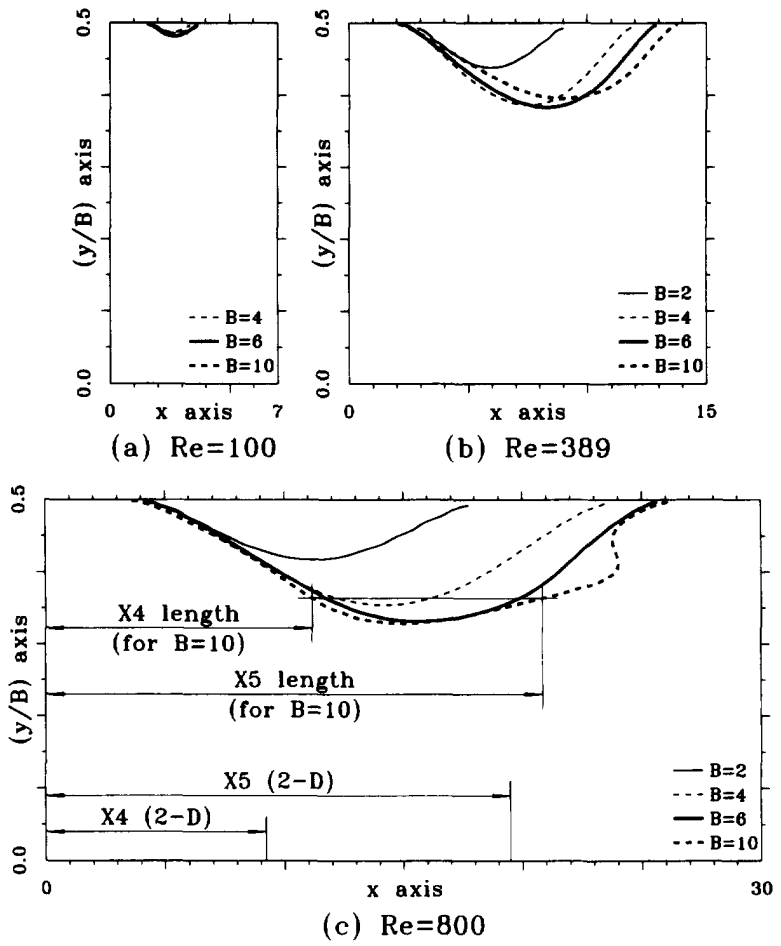

Fig. 9. The computed separation length x_4 and reattachment length x_5 against y for different cases of B and Re. (a) $Re = 100$; (b) $Re = 389$; (c) $Re = 800$.

of graphical visualization of the scalar quantity. The density of helicity or the normalized helicity is frequently chosen in this regard [21]. Due to space considerations, we will concentrate on topological study of skin-friction lines for the surface topology or on streamlines in regions sufficiently distant from the surfaces.

We will examine the flow topology in two areas. The first area is that of the surface topology. In this context, singular points can be classified as saddles and nodal points. Saddle points are defined as singular points which have two real eigenvalues of different signs. The skin-friction line field approaches the saddle point along the negative eigendirection, while it recedes along the positive eigendirection. Nodal points can be further divided into two groups. Nodes (or regular nodal points) are those in association with real eigenvalues of the same sign. Attracting nodes are associated with the negative real eigenvalue, and repelling nodes do the reverse. Foci are also referred to the singular points, whose eigenvalues are, on the other hand, conjugate complex. Depending on the sign of the real part of the eigenvalues, they spiral either in or out of the singular points.

In three dimensions, streamlines approach (recede) a three-dimensional saddle along a plane spanned by two eigenfunctions of the same sign, and recede (approach) from a line having the same direction as the third eigenfunction [25]. Similar to two-dimensional classification of critical points, three-dimensional nodes are those defined as having three real eigenvalues, while irregular nodal points (or spiral saddles) accommodate a pair of conjugate complex eigenvalues and a real eigenvalue. They follow the same rule in classifying critical points, either repelling or attracting nodes and spirals. The topological results presented in Section 6 are rooted in the fundamentals discussed in this section.

6. COMPUTED RESULTS

The problem we consider in this paper consists of expansion in a rectangular water-filled channel with an upstream step and two side walls. This is the so-called 'backward-facing step' problem which was proposed as a comparison exercise by many authors. This has been the subject of intensive two-dimensional study for a wide range of Reynolds numbers. The present study addresses a detailed three-dimensional expansion flow structure behind the step. The geometry for the problem is shown in Fig. 1. The boundary conditions are briefly described as follows: at the upstream inlet we provide discrete fully-developed velocities [26]. At the roof, floor and side wall of the channel the usual no-slip boundary conditions apply. Due to symmetry of the geometry and boundary conditions, only half of the channel is modeled. This assumption has been experimentally verified for the Reynolds numbers considered. Exploiting the experimentally verified symmetry of the flow field, we apply a symmetric boundary condition on the central vertical symmetry plane $y = 0$. How to apply appropriate outflow boundary conditions at the synthetic outlet to avoid numerical disturbances propagated upstream from boundary layers that are attached to the roof, floor and the two side walls is still an open question and has been the focus of many previous studies. According to the work of Kaiktsis *et al.* [3], the sensitivity of the solutions to channel lengths upstream and downstream of the step is, fortunately, not appreciable. In this regard, we prescribe a very simple setting of the outflow boundary conditions at a streamwise plane which is sufficiently away from the step. Numerical experience reveals that the specification of zero

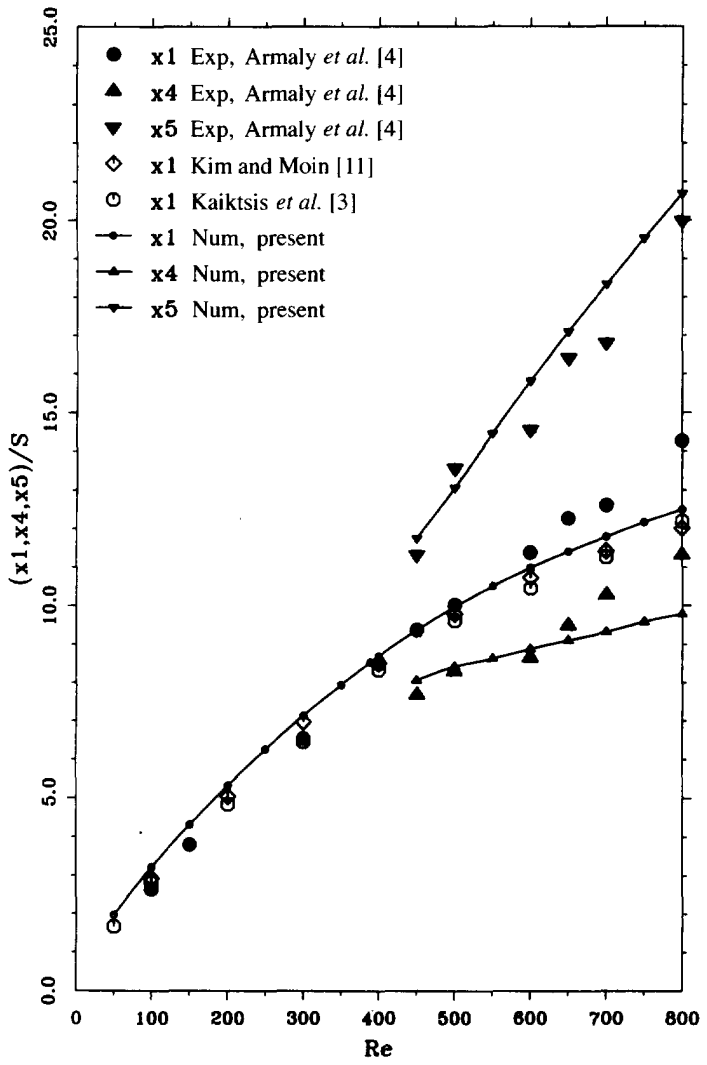

Fig. 10. A comparison study of separation length x_4 and reattachment lengths x_1 and x_5 with other two-dimensional results.

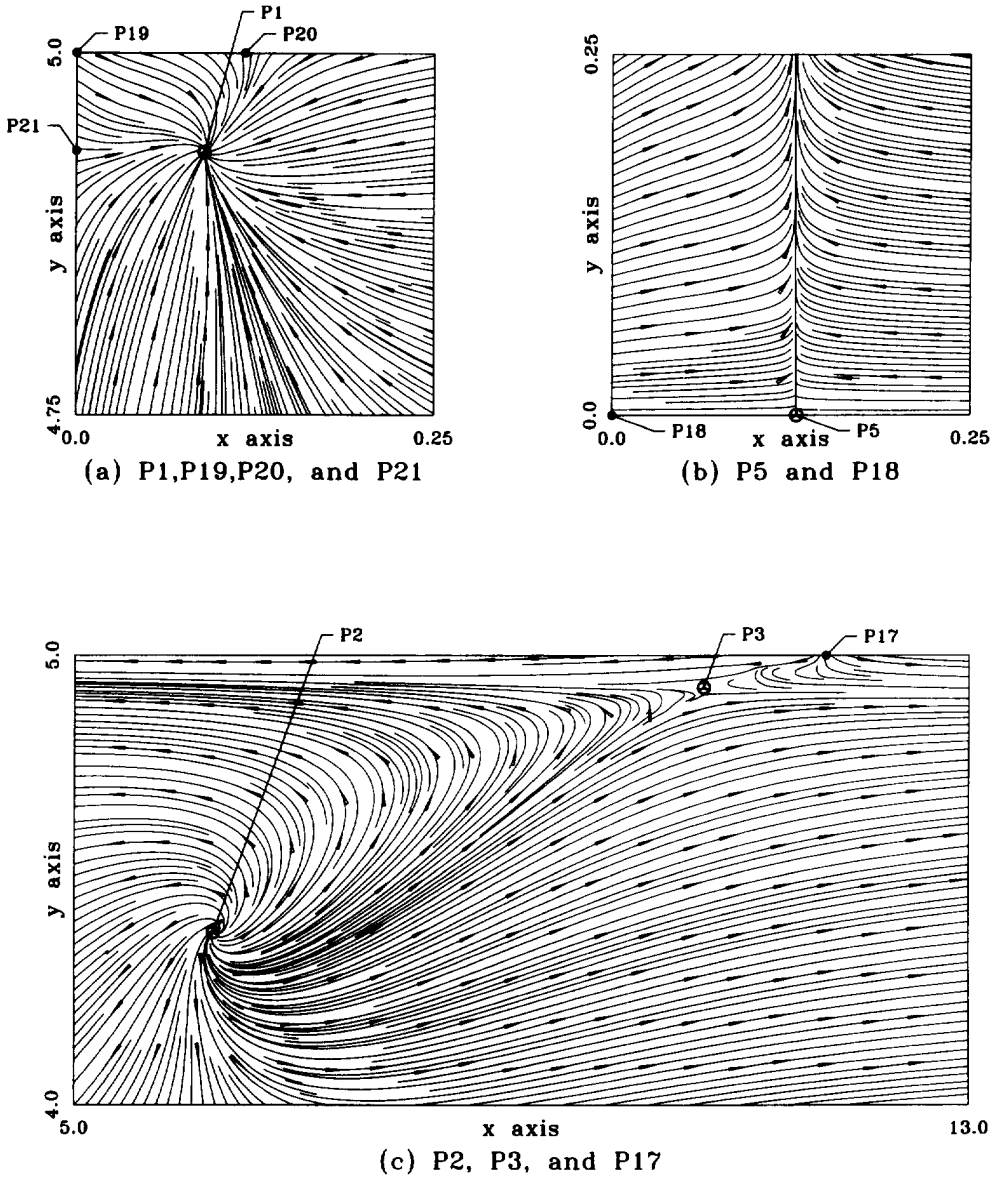

Fig. 11. A close-up look at singularities present on the floor of the channel for the case of $Re = 389$, $B = 10$.

gradients for velocity components at the outlet is sufficient to compensate the potential loss of accuracy.

In step flows, it is crucial to resolve high gradient boundary-layer profiles in regions near solid walls and curved streamlines around the expansion corner. We, therefore, stretch meshes near all walls, the step plane, regions of flow reversal, and the approach to the outlet plane. As Fig. 3 reveals, for the case of $Re = 389$, half of the channel is covered with graded mesh points $80 \times 17 \times 40$ for $B = 2$ but $80 \times 37 \times 40$ for $B = 10$.

The global flow feature pertinent to the problem, as illustrated in Fig. 1, is the flow separation from the step corner, followed by a downstream reattachment on a solid surface. Bearing in mind that there is marked change in the shear stress distribution and the heat transfer rate in the reversal flow, detecting the reattachment location is, thus, important for identification of the range of flow reversals. The clarification of separation and attachment lines poses no difficulty in two-dimensional analyses. The determination of three-dimensional flow separation/attachment is not a trivial task to achieve. This has been a matter of much debate in recent decades. Of the numerous attempts to enhance flow visualization, topological studies on a three-dimensional vector

field and flow visualizations of helicity lend themselves to precise mathematical formulation. It is this rigorous analysis that motivates us to apply the theory of the topology of continuous vectors to improve three-dimensional flow visualization. This also facilitates the identification of singular points of different characters and, thus, helps to sketch the flow structure. Given that a pattern of skin-friction lines on a body surface is analogous to limiting streamlines (as calculated from the projection of the velocity field onto planes near the roof, floor and end wall of the channel, on a plane which is immediately adjacent to that surface) we plot limiting streamlines on the end wall and roof as well as the floor of the channel. In Legendre's terminology, flow patterns thus obtained are considered to be trajectories having properties consistent with those rendered from experimental oil-streak lines.

To give a global view of the expansion flow over a step, we begin by plotting limiting streamlines, namely at $z = 0.9999$, -0.9423, $y = 4.9999$, and $x = 10^{-4}$ for $Re = 389$ in the channel of width 10, as shown in Fig. 4. As Fig. 4 indicates, a singular point, classified as the saddle, is shown on a plane adjacent to the end wall. On planes in the direction normal to the end wall, we plot streamlines. We then collected the computed saddles at different y planes and plot them in Fig. 5. This line is confined only to a narrow region near the end wall and does not extend to the core of the flow. Lines passing through saddle points are only those referred to as attachment and separation lines. These two lines appear to act as barriers in the field. On each of these two critical lines, the direction changes sign. Both directions point towards the saddle and point away from the saddle on the other. As shown in the close-up plot in Fig. 5, there exists a repelling focus above the saddle. Notable here, is the presence of a global line of separation (or a line of closed separation of Wang [27], or simply a primary separation type II of Champman [28]) in the channel (Fig. 5). Using the terminology of Tobak and Peakes [29], such a cluster of global separation lines serves as a potential mechanism leading to global flow separation.

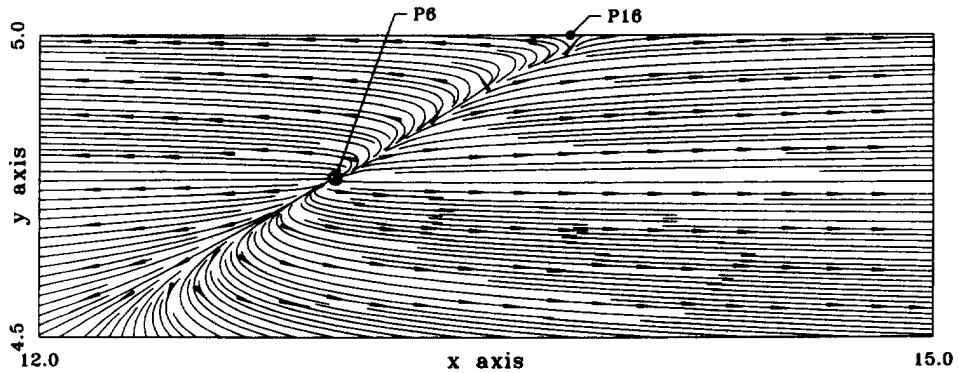

(a) P6 and P16

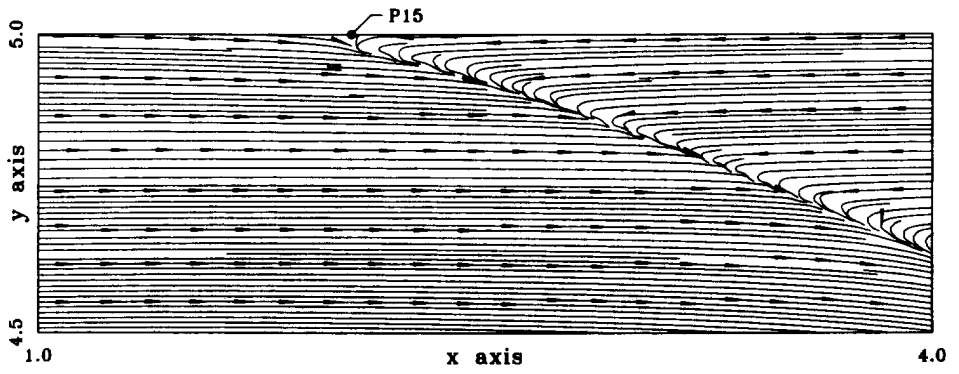

(b) P15

Fig. 12. A close-up look at singularities present on the roof of the channel for the case of $Re = 389$, $B = 10$.

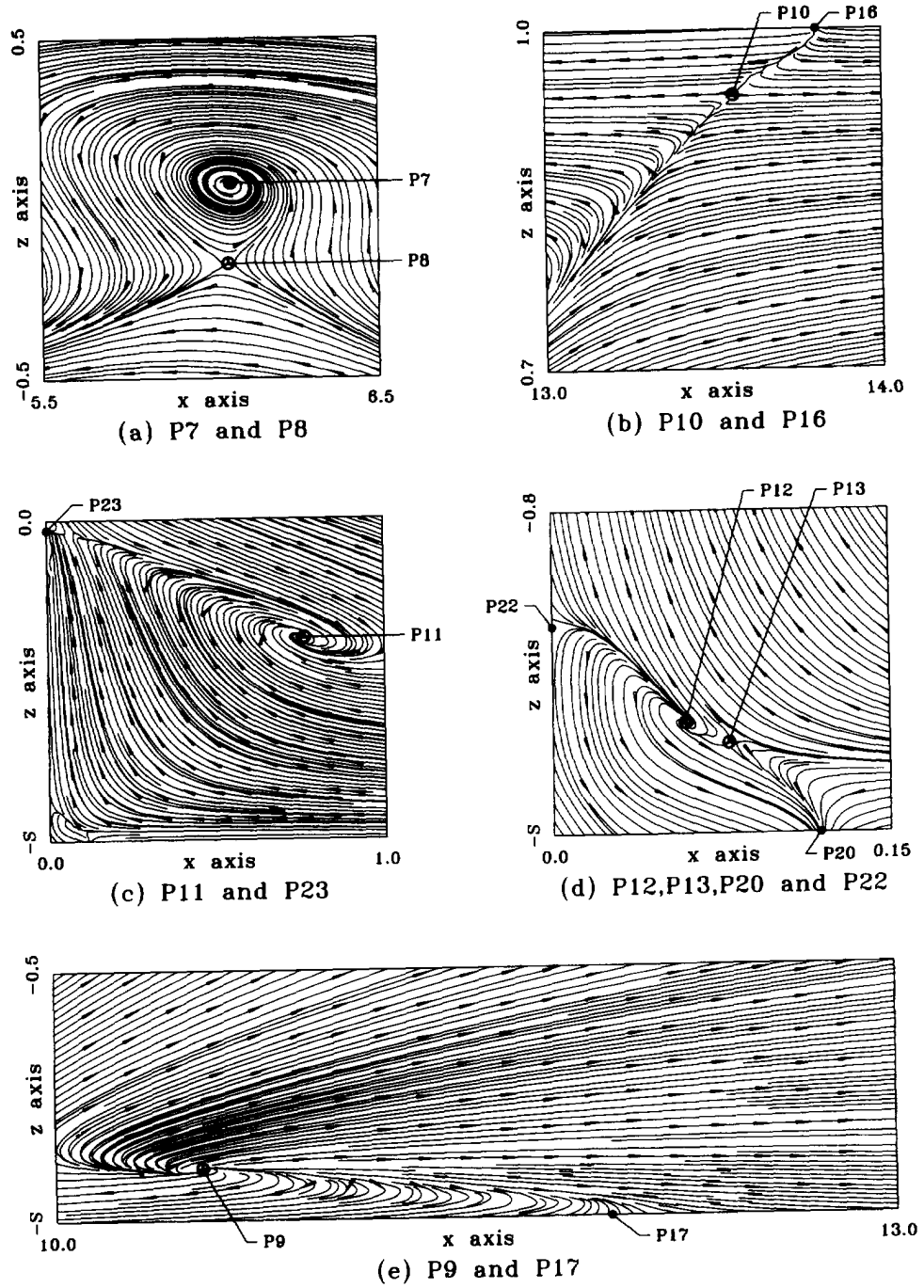

Fig. 13. A close-up look at singularities present on the side wall of the channel for the case of $Re = 389$, $B = 10$.

To allow for determination of three-dimensional flow separation and reattachment, one may use surface flow topology as a guide for visualizing the flow recirculation. We label the line of separation as the one to which streamlines converge. On the other hand, from either side of a line of attachment, streamlines tend to diverge. According to this definition, a clear picture indicating the presence of flow reattachment to the floor is seen in Fig. 6 across the half span. We plot the reattachment length, x_1, as measured from the step, against spans in Fig. 7 for Reynolds numbers 100, 389, and 800. To allow for comparison with x_1 rendered from two-dimensional analysis, we also plot lengths of x_1. In the presence of a primary recirculation eddy behind the step, convex curved streamlines engender flow separation from the roof in the streamwise location where the separated flow reattaches to the

floor. The presence of a secondary separation zone near the roof is a consequence of an adverse pressure gradient caused by sudden expansion at the step edge. The flow recovers downstream and reattaches to the upper wall. For example, the flow separation–reattachment feature is clearly identified in Fig. 8. Exploiting the mathematically appealing topological theory, we can also plot the separation length x_4 and the reattachment length x_5 in Fig. 9. As is the case with the plot of x_1, lengths x_4 and x_5 are also measured from the step. These values are plotted against the spans for the three investigated Reynolds numbers. Beyond a small Reynolds number, say $Re = 100$, evidence of the separation–reattachment flow on the roof is seen in Fig. 9. This clearly reveals the development of three-dimensional flow, in contrast to the results of two-dimensional analysis where the presence of a secondary eddy is reported at Reynolds numbers as high as 450 (Fig. 10). Topological maps of inferred flow patterns for each case considered reveal that separation–reattachment comes into play only in flow regions near the end wall. Even for a Reynolds number as high as 800, there is no tendency for the formation of separation–reattachment on the symmetry plane over the range of investigated spans. Further work is in progress to reproduce the experimental work of Armaly [4], whose experiment was conducted in a channel with a width of 36. Questions as to whether the secondary flow emerges near the symmetry plane will be the focus of future study. Downstream of the roof eddy, there is a gradual flow development into a parabolic profile.

In recirculating flows, flow reversal or recirculation frequently involves the simultaneous existence of several singular points. For example, one can clearly see singular points in the close-up plots. As Figs 11–13 indicate, singular points of different classes are visible. For the flow conditions under investigation, we have prepared statistics, shown in Tables 1–4, which summarize the relevant singular points, according to the classifications discussed in Section 5.

Table 1. The spatial locations and classifications of singular points for the case of $Re = 389$ and $B = 10$

No.	L/A/B	(x,y,z) Coordinates
$Re = 389$, $B = 10$		
P1	1/4/4	(0.0891,4.9362, − 0.9423)
P2	1/3/5	(6.2822,4.3812, − 0.9423)
P3	1/1/6	(10.699,4.9281, − 0.9423)
P4	1/2/6	(8.5469,0.0000, − 0.9423)
P5	1/1/6	(0.1257,0.0000, − 0.9423)
P6	2/1/3	(13.002,4.7636, 1.0000)
P7	3/4/4	(6.0646,5.0000, 0.0669)
P8	3/1/6	(6.0489,5.0000, − 0.1612)
P9	3/1/3	(10.547,5.0000, − 0.8560)
P10	3/2/6	(13.558,5.0000, 0.9430)
P11	3/4/4	(0.7636,5.0000, − 0.3572)
P12	3/1/3	(0.0445,5.0000, − 0.8874)
P13	3/1/6	(0.0832,5.0000, − 0.9120)
P14	4/1/3	(0.0000,0.0000, − 0.8148)
P15	5/1/1	(2.0713,5.0000, 1.0000)
P16	5/1/1	(13.797,5.0000, 1.0000)
P17	5/1/1	(11.914,5.0000, − 0.9423)
P18	5/1/1	(0.0000,0.0000, − 0.9423)
P19	5/1/1	(0.0000,5.0000, − 0.9423)
P20	5/2/1	(0.1150,5.0000, − 0.9423)
P21	5/2/1	(0.0000,4.9386, − 0.9423)
P22	5/2/1	(0.0000,5.0000, − 0.8553)
P23	5/1/1	(0.0000,5.0000, − 0.0294)

Singular points in 3D backward-facing step channel flows
< L: Location Definitions >
L = 1: $z =$ − Sh bottom wall plane
L = 2: $z = h$ top wall plane
L = 3: $y = 0.5B$ side wall plane
L = 4: $x = 0$ step wall plane
L = 5: Intersections between above planes
< A/B Type Definitions >
Type A
A = 1: Repelling–Node–Saddle
A = 2: Attracting–Node–Saddle
A = 3: Repelling–Spiral–Saddle
A = 4: Attracting–Spiral–Saddle
Type B (Skin friction type)
B = 1: On–Multiple–No–Slip
B = 2: Attracting–Node2d
B = 3: Repelling–Node2d
B = 4: Attracting–Spiral2d
B = 5: Repelling–Spiral2d
B = 6: Saddle

Table 2. The spatial locations and classifications of singular points for different spans computed for the case of $Re = 100$. (For definitions of L, A and B, please see Table 1.)

L/A/B	(x,y,z) Coordinates
$Re = 100$, $B = 2$	
1/2/2	(0.0611,0.9327, − 0.9423)
1/1/6	(0.0603,0.6774, − 0.9423)
1/1/3	(2.3121,0.0000, − 0.9423)
1/2/2	(0.0842,0.0000, − 0.9423)
3/2/6	(2.7163,1.0000, − 0.7732)
3/1/3	(2.7704,1.0000, − 0.8092)
4/2/6	(0.0000,0.0000, − 0.8656)
4/1/3	(0.0000,0.6382, − 0.8720)
5/2/1	(2.9857,1.0000, − 0.9423)
5/2/1	(0.0000,0.0000, − 0.9423)
5/2/1	(0.0000,1.0000, − 0.9423)
5/1/1	(0.0960,1.0000, − 0.9423)
5/1/1	(0.0000,0.6076, − 0.9423)
5/1/1	(0.0000,1.0000, − 0.8685)
5/2/1	(0.0000,1.0000, − 0.0450)
$Re = 11$, $B = 4$	
1/2/2	(0.0628,1.9399, − 0.9423)
1/1/6	(0.0514,1.7902, − 0.9423)
1/3/5	(2.6020,1.2904, − 0.9423)
1/2/6	(2.8300,0.0000, − 0.9423)
1/2/2	(0.0896,0.0000, − 0.9423)
2/3/5	(2.9768,1.9592, 1.0000)
3/2/6	(2.7325,2.0000, − 0.5510)
3/1/3	(3.2383,2.0000, − 0.8576)
4/2/6	(0.0000,0.0000, − 0.8560)
4/1/3	(0.0000,1.7580, − 0.8783)
5/2/1	(1.8392,2.0000, 1.0000)
5/2/1	(3.3485,2.0000, 1.0000)
5/2/1	(3.3840,2.0000, − 0.9423)
5/2/1	(0.0000,0.0000, − 0.9423)
5/2/1	(0.0000,2.0000, − 0.9423)
5/1/1	(0.0971,2.0000, − 0.9423)
5/1/1	(0.0000,1.7335, − 0.9423)
5/1/1	(0.0000,2.0000, − 0.8737)
5/2/1	(0.0000,2.0000, − 0.0477)
$Re = 100$, $B = 6$	
1/2/2	(0.0641,2.9421, − 0.9423)
1/1/6	(0.0499,2.8154, − 0.9423)
1/3/5	(2.6624,2.2586, − 0.9423)
1/2/6	(3.4411,2.9844, − 0.9423)
1/2/6	(2.9641,0.0000, − 0.9423)
1/2/2	(0.0902,0.0000, − 0.9423)
2/3/5	(3.2587,2.9269, 1.0000)
3/2/6	(2.7013,3.0000, − 0.4872)
3/1/3	(3.2956,3.0000, − 0.8576)
3/2/6	(3/6317,3.0000, 0.9807)
4/2/6	(0.0000,0.0000, − 0.8547)
4/1/3	(0.0000,2.7826, − 0.8791)
5/2/1	(1.6513,3.0000, 1.0000)
5/1/1	(3.6813,3.0000,1.0000)
5/1/1	(3.4442,3.0000, − 0.9423)
5/2/1	(0.0000,0.0000, − 0.9423)
5/2/1	(0.0000,3.0000, − 0.9423)
5/1/1	(0.0982,3.0000, − 0.9423)
5/1/1	(0.0000,2.7595, − 0.9423)
5/1/1	(0.0000,3.0000, − 0.8751)
5/2/1	(0.0000,3.0000, − 0.0481)
$Re = 100$, $B = 10$	
1/2/2	(0.0651,4.9436, − 0.9423)
1/1/6	(0.0490,4.8265, − 0.9423)
1/3/5	(2.6097,4.2265, − 0.9423)
1/2/6	(3.4295,4.9822, − 0.9423)
1/2/6	(3.0364,0.0000, − 0.9423)
1/2/2	(0.0894,0.0000, − 0.9423)
2/3/5	(3.3946,4.9071,1.0000)
3/2/6	(2.6610,5.0000, − 0.4446)
3/1/3	(3.2965,5.0000, − 0.8567)
3/2/6	(3.7523,5.0000,0.9783)
4/2/6	(0.0000,0.0000, − 0.8566)
4/1/3	(0.0000,4.7959, − 0.8792)
5/2/1	(1.5552,5.0000,1.0000)
5/1/1	(3.8126,5.0000,1.0000)
5/1/1	(3.4422,5.0000, − 0.9423)
5/2/1	(0.0000,0.0000, − 0.9423)
5/2/1	(0.0000,5.0000, − 0.9423)
5/1/1	(0.0987,5.0000, − 0.9423)
5/1/1	(0.0000,4.7731, − 0.9423)
5/1/1	(0.0000,5.0000, − 0.8765)
5/2/1	(0.0000,5.0000, − 0.0458)

Table 3. The spatial locations and classifications of singular points for different spans computed for the case of $Re = 389$. (For definitions of L, A and B, please see Table 1.)

L/A/B	(x,y,z) Coordinates
$Re = 389$, $B = 2$	
1/4/4	(0.1489,0.9440, − 0.9423)
1/1/3	(6.8621,0.2767, − 0.9423)
1/2/6	(6.8897,0.0000, − 0.9423)
1/2/6	(0.1031,0.0000, − 0.9423)
2/3/5	(8.0972,0.9435, 1.0000)
3/2/2	(4.0397,1.0000, 0.9314)
3/2/6	(6.7402,1.0000, − 0.5576)
3/1/3	(8.8814,1.0000, − 0.8755)
3/1/6	(3.7971,1.0000, 0.9427)
3/4/4	(0.9837,1.0000, − 0.3371)
3/1/3	(0.0256,1.0000, − 0.8683)
3/1/6	(0.1597,1.0000, − 0.9163)
4/1/3	(0.0000,0.0000, − 0.7677)
5/2/1	(2.8773,1.0000, 1.0000)
5/2/1	(9.0197,1.0000, 1.0000)
5/2/1	(9.3873,1.0000, − 0.9423)
5/1/1	(0.0000,0.0000, − 0.9423)
5/1/1	(0.0000,1.0000, − 0.9423)
5/2/1	(0.1859,1.0000, − 0.9423)
5/2/1	(0.0000,0.9526, − 0.9423)
5/2/1	(0.0000,1.0000, − 0.8536)
5/1/1	(0.0000,1.0000, − 0.0337)
$Re = 389$, $B = 4$	
1/4/4	(0.0990,1.9389, − 0.9423)
1/3/5	(6.9872,1.3531, − 0.9423)
1/2/6	(10.490,1.9526, − 0.9423)
1/2/6	(8.2421,0.0000, − 0.9423)
1/2/6	(0.1472,0.0000, − 0.9423)
2/3/5	(10.896,1.8580, 1.0000)
3/4/4	(6.0556,2.0000, 0.5830)
3/2/6	(6.5264,2.0000, − 0.3951)
3/3/5	(10.229,2.0000, − 0.8713)
3/2/6	(11.589,2.000, 0.9547)
3/1/6	(2.4682,2.0000, 0.9831)
3/4/4	(0.8635,2.0000, − 0.3781)
4/1/3	(0.0000,0.0000, − 0.6983)
5/2/1	(2.4347,2.0000, 1.0000)
5/1/1	(11.931,2.0000, 1.0000)
5/1/1	(10.962,2.0000, − 0.9423)
5/1/1	(0.0000,0.0000, − 0.9423)
5/1/1	(0.0000,2.0000, − 0.9423)
5/2/1	(0.1215,2.0000, − 0.9423)
5/2/1	(0.0000,1.9321, − 0.9423)
5/2/1	(0.0000,2.0000, − 0.8538)
5/1/1	(0.0000,2.0000, − 0.0341)
$Re = 389$, $B = 6$	
1/4/4	(0.0897,2.9359, − 0.9423)
1/3/5	(6.7436,2.3605, − 0.9423)
1/1/6	(10.718,2.9427, − 0.9423)
1/2/6	(8.4390,0.0000, − 0.9423)
1/1/6	(0.1432,0.0000, − 0.9423)
2/1/3	(11.945,2.8026, 1.0000)
3/4/4	(6.2274,3.0000, 0.3758)
3/1/6	(6.3630,3.0000, − 0.3160)
3/3/5	(10.492,3.0000, − 0.8608)
3/2/6	(12.617,3.0000, 0.9463)
3/4/4	(0.8019,3.0000, − 0.3676)
4/1/3	(0.0000,0.0000, − 0.7469)
5/1/1	(2.2705,3.0000, 1.0000)
5/1/1	(12.905,3.0000, 1.0000)
5/1/1	(11.431,3.0000, − 0.9423)
5/1/1	(0.0000,0.0000, − 0.9423)
5/1/1	(0.0000,3.0000, − 0.9423)
5/2/1	(0.1150,3.0000, − 0.9423)
5/2/1	(0.0000,2.9349, − 0.9423)
5/2/1	(0.0000,3.0000, − 0.8545)
5/1/1	(0.0000,3.0000, − 0.0329)

Table 4. The spatial locations and classifications of singular points for different spans computed for the case of $Re = 800$. (For definitions of L, A and B, please see Table 1.)

L/A/B	(x,y,z) Coordinates	L/A/B	(x,y,z) Coordinates
$Re = 800$, $B = 2$		$Re = 800$, $B = 6$	
1/4/4	(0.4899, 0.9147, −0.9423)	1/4/4	(0.0841, 2.8800, −0.9423)
1/1/3	(13.266, 0.2909, −0.9423)	1/3/5	(11.325, 2.4315, −0.9423)
1/2/6	(13.378, 0.0000, −0.9423)	1/1/6	(18.894, 2.9301, −0.9423)
1/2/6	(0.1861, 0.0000, −0.9423)	1/2/6	(15.437, 0.0000, −0.9423)
2/3/5	(15.855, 0.9340, 1.0000)	1/2/6	(0.6029, 0.0000, −0.9423)
3/4/4	(9.1026, 1.0000, 0.8578)	2/1/3	(24.009, 2.8200, 1.0000)
3/2/6	(12.262, 1.0000, −0.5235)	2/2/2	(6.1191, 2.8381, 1.0000)
3/1/3	(17.558, 1.0000, −0.8743)	3/4/4	(10.900, 3.0000, 0.0693)
3/1/6	(5.2200, 1.0000, 0.9771)	3/1/6	(10.794, 3.0000, −0.2450)
3/4/4	(1.8574, 1.0000, −0.3675)	3/1/3	(18.603, 3.0000, −0.8590)
3/3/5	(0.0411, 1.0000, −0.8682)	3/2/6	(24.846, 3.0000, 0.9245)
3/1/6	(0.5524, 1.0000, −0.9048)	3/4/4	(1.2067, 3.0000, −0.5877)
4/1/3	(0.0000, 0.0000, −0.6085)	4/1/3	(0.0000, 0.0000, −0.4157)
5/2/1	(4.7391, 1.0000, 1.0000)	4/1/6	(0.0000, 2.8689, −0.9068)
5/2/1	(17.770, 1.0000, 1.0000)	4/1/3	(0.0000, 2.9647, −0.8532)
5/2/1	(18.684, 1.0000, −0.9423)	5/1/1	(4.1383, 3.0000, 1.0000)
5/1/1	(0.0000, 0.0000, −0.9423)	5/1/1	(25.670, 3.0000, 1.0000)
5/1/1	(0.0000, 1.0000, −0.9423)	5/1/1	(21.723, 3.0000, −0.9423)
5/2/1	(0.5932, 1.0000, −0.9423)	5/2/1	(0.0000, 0.0000, −0.9423)
5/2/1	(0.0000, 0.9417, −0.9423)	5/1/1	(0.0000, 3.0000, −0.9423)
5/2/1	(0.0000, 1.0000, −0.8478)	5/2/1	(0.0548, 3.0000, −0.9423)
5/1/1	(0.0000, 1.0000, −0.0278)	5/2/1	(0.0000, 2.8302, −0.9423)
$Re = 800$, $B = 4$		5/2/1	(0.0000, 3.0000, −0.8273)
1/4/4/	(0.8399, 1.7455, −0.9423)	5/1/1	(0.0000, 3.0000, −0.0246)
1/3/5	(12.530, 1.3636, −0.9423)	$Re = 800$, $B = 10$	
1/1/6	(20.427, 1.9479, −0.9423)	1/2/2	(0.0804, 4.9123, −0.9423)
1/2/6	(15.739, 0.0000, −0.9423)	1/3/5	(9.4399, 4.4510, −0.9423)
1/2/6	(0.4985, 0.0000, −0.9423)	1/1/6	(15.190, 4.9314, −0.9423)
2/3/5	(21.456, 1.8481, 1.0000)	1/2/6	(15.257, 0.0000, −0.9423)
2/2/2	(7.1190, 1.8066, 1.0000)	1/1/6	(0.6748, 0.0000, −0.9423)
3/4/4	(11.284, 2.0000, 0.4552)	1/1/3	(0.0295, 0.0000, −0.9423)
3/1/6	(11.497, 2.0000, −0.3783)	2/1/3	(24.881, 4.8294, 1.0000)
3/3/5	(19.818, 2.0000, −0.8627)	2/2/2	(4.9493, 4.8573, 1.0000)
3/2/6	(22.730, 2.0000, 0.9455)	2/1/6	(5.4426, 4.7827, 1.0000)
3/4/4	(1.6325, 2.0000, −0.4887)	2/1/6	(22.892, 3.8250, 1.0000)
3/1/3	(0.1968, 2.0000, −0.8518)	2/4/4	(13.085, 3.3625, 1.0000)
4/1/3	(0.0000, 0.0000, −0.4303)	3/1/3	(15.424, 5.0000, −0.8733)
5/1/1	(4.2787, 2.0000, 1.0000)	3/2/6	(25.320, 5.0000, 0.9015)
5/1/1	(23.549, 2.0000, 1.0000)	3/4/4	(1.0677, 5.0000, −0.4621)
5/1/1	(21.723, 2.0000, −0.9423)	4/1/3	(0.0000, 0.0000, −0.4091)
5/2/1	(0.0000, 0.0000, −0.9423)	5/1/1	(3.6407, 5.0000, 1.0000)
5/2/1	(0.0000, 2.0000, −0.9423)	5/1/1	(26.298, 5.0000, 1.0000)
5/1/1	(0.1610, 2.0000, −0.9423)	5/1/1	(22.913, 5.0000, −0.9423)
5/1/1	(0.9119, 2.0000, −0.9423)	5/2/1	(0.0000, 0.0000, −0.9423)
5/1/1	(0.0000, 1.8617, −0.9423)	5/1/1	(0.0000, 5.0000, −0.9423)
5/1/1	(0.0000, 2.0000, −0.8184)	5/2/1	(0.0940, 5.0000, −0.9423)
5/1/1	(0.0000, 2.0000, −0.0271)	5/2/1	(0.0000, 4.8955, −0.9423)
		5/2/1	(0.0000, 5.0000, −0.8476)
		5/1/1	(0.0000, 5.0000, −0.0187)

7. CONCLUSIONS

A numerical method formulated in a three-dimensional context has been analytically verified, with an emphasis on the rate of convergence. The intent of this study is to explore the vortical flow structure present in the channel with a backward-facing step. Given that flow reversal involves the simultaneous existence of several singular points, we are motivated to adopt the topological theory on skin-friction line fields as a guide for exploring the physically realistic flow field.

By carefully finding singular points to display and eigendirections to integrate, we can visualize the kinematically possible flow. Examination on the computed skin-friction lines has revealed the presence of saddles, nodal points and other half-nodes of separation and attachment, from which the global flow structure can be sketched. Use of a rigorous mathematical foundation has facilitated the determination of a separation line on the floor and the separation, proceeding continuously with the attachment line, on the roof of the channel. To extend our knowledge of the flow physics inside a channel having a backward-facing step, we have carried out a parametric study by varying Reynolds numbers and spans, with values not greater than 800 and 10, respectively. The conclusions drawn from this parametric study are two-fold. Regardless of the values of the Reynolds numbers, flow separation–attachment occurs on the roof of the channel but is confined only to the end wall region. Interior saddles are also detected. A collection of them forms a global

line of separation which suggests a mechanism for the development of a truly three-dimensional flow to the subsequent flow instabilities on increase of the Reynolds numbers.

Acknowledgement—This work was supported by the National Science Council under Grant NCHC 85-04-004.

REFERENCES

1. Lighthill, M., Attachment and separation in three-dimensional flow. In *Laminar Boundary Layers*, Vol. 2(6), ed. L. Rosenhead, II. Oxford University Press, 1963, pp. 72–82.
2. Morgan, K., Periaux, J. and Thomasset, F., ed., *Analysis of Laminar Flow over a Backward Facing Step, A GAMM-Workshop*. Friedr View and Sohn, Germany, 1984.
3. Kaiktsis, L., Karniadakis, G. E. M. and Orszag, S. A.,, Onset of three-dimensionality, equilibria, and early transition in flow over a backward-facing step. *J. Fluid Mech.*, 1991, **231,** 501–528.
4. Armaly, B. F., Durst, F., Pereira, J. C. F. and Schonung, B., Experimental and theoretical investigation of backward-facing step. *J. Fluid Mech.*, 1983, **127,** 473–496.
5. Goldstein, R. J., Eriksen, V. L., Olson, R. M. and Eckert, E. R. G.,, Laminar separation reattachment, and transition of flow over a downward-facing step. *Trans. ASME D: J. Basic Engng*, 1970, **92,** 732–741.
6. Shih, C. and Ho, C.-M., Three-dimensional recirculation flow in a backward facing step. *ASME J. Fluids Engng*, 1994, **116,** 228–232.
7. Yoo, J. Y. and Baik, S. J., Redeveloping turbulent boundary layer in the backward-facing step flow. *ASME J. Fluids Engng*, 1992, **114,** 522–529.
8. Ötiigen, M. V., Expansion ratio effects on the separated shear layer and reattachment downstream of a backward-facing step. *Experiments in Fluids*, 1991, **10,** 273–280.
9. Papadvpoulos, G. and Ötiigen, M. V., Separating and reattaching flow structure in a suddenly expanding rectangular duct. *J. Fluids Engng*, 1995, **117,** 17–23.
10. Kim, J., Kline, S. J. and Johnston, J. P., Investigation of a reattaching turbulent shear layer: flow over a backward-facing step. *ASME J. Fluids Engng*, 1980, **102,** 302–308.
11. Kim, J. and Moin, P., Applications of a fractional-step method to incompressible Navier–Stokes equations. *J. Comput. Phys.*, 1985, **59,** 308–323.
12. Ku, H. C., Hirsh, R. S., Taylor, T. D. and Rosenburg, A. P., A pseudo-spectral matrix element method for solution of three-dimensional incompressible flows and its parallel implementation. *J. Comput. Phys.*, 1989, **83,** 260–291.
13. Kwak, D. and Chang, J. L. C., A three-dimensional incompressible Navier–Stokes flow solver. Part 1-2NS3D code. CFD Workshop, University of Tennessee Space Institute, Tullahoma, TN, 1985.
14. Williams, P. T. and Baker, A. J., Incompressible computational fluids dynamics and the continuity constraint method for the three-dimensional Navier–Stokes equations. *Numerical Heat Transfer, Part B*, 1996, **29,** 137–273.
15. Ikohagi, T., Shin, B. R. and Daiguji, H., Application of an implicit time-marching scheme to a three-dimensional incompressible flow problem in curvilinear coordinate systems. *Comput. Fluids*, 1992, **21,** 163–175.
16. Williams, P. T. and Baker, A. J., Numerical simulations of laminar flow over a 3D backward-facing step. *Int. J. Numer. Meth. Fluids*, submitted.
17. Harlow, F. H. and Welch, J. E., Numerical calculation of time-dependent viscous incompressible flow of fluid with free surface. *Phys. Fluids*, 1965, **8,** 2182–2189.
18. Patankar, S. V., *Numerical Heat Transfer and Fluid Flow*. Hemisphere, New York, 1980.
19. Leonard, B. P., A stable and accurate convective modeling procedure based on quadratic upstream interpolation. *Comput. Methods Appl. Mech. Engng*, 1979, **19,** 59–98.
20. Ethier, C. R. and Steinman, D. A., Exact fully 3D Navier–Stokes solutions for benchmarking. *Int. J. Numer. Meth. Fluids*, 1994, **19,** 369–375.
21. Levy, Y., Degani, D. and Seginer, A., Graphical visualization of vortical flows by means of helicity. *AIAA J.*, 1990, **28,** 1347–1352.
22. Legendre, R., Séparation de courant l'écoulement laminaire tridimensionnel. *Rech. Aéro.*, 1956, **54,** 3–8.
23. Yates, L. A. and Chapman, G. T., Streamlines, vorticity lines, and vortices around three-dimensional bodies. *AIAA J.*, 1992, **30,** 1819–1826.
24. Poincare, H., Surles courbes defines par une equation differentiette. *J. Math.*, 1875, **1,** 167.
25. Bancroft, G., Merritt, F., Plessel, T., Kelaita, P., McCabe, R. and Globus, A., FAST: A multi-processing environment for visualization of CFD. *Proc. Visualization '90, IEEE Computer Society*, San Francisco, CA, 1990.
26. White, F. M., *Viscous Fluid Flow*, 2nd Edn. McGraw-Hill, New York, 1991.
27. Wang, K. C., Boundary layer over a blunt body at high incidence with an open type of separation. *Proceedings of the Royal Society of London, Series A*, 1974, **340,** pp. 33–35.
28. Chapman, G. T., Topological classification of flow separation on three dimensional bodies. AIAA paper, 86-0485, 1986.
29. Tobak, M. and Peaks, D. J., Topology of three-dimensional separated flows. *Ann. Rev. Fluid Mech.*, 1982, **14,** 61–85.